DIELECTRIC CONSTANT CONSTRAINTS OF SUSPECTED SURFICIAL WATER-ICE REGIONS IN THE LUNAR SOUTH POLE. T. P. Himani[1,2], N. T. Dutton[3], G. W. Patterson[4], and K. W. Lewis[1]. [1]Dept. of Earth and Planetary Science, Johns Hopkins Univ., Baltimore, MD (thimani1@jhu.edu), [2]Remote Sensing Division, U.S. Naval Research Laboratory, Washington, D.C. [3]Space Analysis and Modeling Group, Johns Hopkins University Applied Physics Laboratory, Laurel, MD. [4]Planetary Exploration Group, Johns Hopkins University Applied Physics Laboratory, Laurel, MD

Introduction: The Mini-RF instrument on board the Lunar Reconnaissance Orbiter (LRO) is a dual-frequency synthetic aperture radar (SAR) operating at both S-band (12.6 cm) and X-band (4.2 cm) [1]. One of the primary objectives of the instrument has been to characterize the presence and distribution of water-ice in the permanently shadowed regions (PSR) of the lunar north and south poles. Recent measurements of surficial water ice made using the Moon Minerology Mapper (M^3) [2] were combined using data from the Lunar Orbiter Laser Altimeter (LOLA), Diviner, Lunar Prospector Neutron Spectrometer (LPNS), and the Kaguya Laser ALTimeter (LALT) in order to identify PSRs with the highest abundance of volatiles [3]. A total of 169 water-ice bearing PSRs were identified, with Faustini, Shoemaker, Haworth, and Sverdrup being among 37 regions identified as high interest. While radar data was not used as part of identifying the above regions, data from Mini-RF can provide additional insights and constraints on surface and subsurface properties which are indicative of surface exposed water-ice volatiles. Prior work in this area has generated curve fits to determine crater diameter bounds which can maximize detectability of water-ice and constrain its electrical properties (such as dielectric constant) at S-band [4].

In this work, we examine the four high-interest PSR regions stated above at X-band and invert their dielectric properties to determine if they are consistent with established modeling/theory. These inversions are also part of a radar processing pipeline currently in development to impose additional constraints (scattering decomposition, CPR, etc.) on current and future PSRs suspected to contain water-ice.

Dielectric Constant Inversion Method: A number of theoretical and empirical models exist for inverting the dielectric constant of the lunar surface/subsurface [5, 6]. These models differ based on how the lunar terrain is defined and the expected radar penetration depth based the selected frequency. At X-band wavelengths and Mini-RF incidence angles (~49°) contributions from subsurface and subsurface-volume scattering are negligible [7] and thus surface scattering is mainly responsible for the returned signal to the radar. For sufficiently rough surfaces at the operating wavelength, the incident wave is scattered evenly in all directions [8].

Recently, a dielectric constant inversion model was developed which can directly take in the measured LH and LV radar returns from Mini-RF (as opposed to assuming LH and LV are equivalent to HH and HV respectively) [9]. This method derives the ratio of Fresnel reflection coefficients for horizontal and vertical polarization based on a three-component hybrid-pol decomposition technique. While this type of decomposition can take into account surface-scattering, dihedral-scattering, and volume-scattering, only the surface scattering is considered. The ratio of Fresnel reflection coefficients is then related to the real part of the dielectric constant using the following equation:

$$\beta = \frac{R_H}{R_V} = \frac{\dfrac{\cos\theta_i - \sqrt{\epsilon_r - \sin^2\theta_i}}{\cos\theta_i + \sqrt{\epsilon_r - \sin^2\theta_i}}}{\dfrac{(\epsilon_r - 1)\{\sin^2\theta_i - \epsilon_r(1 + \sin^2\theta_i)\}}{\left(\epsilon_r\cos\theta_i + \sqrt{\epsilon_r - \sin^2\theta_i}\right)^2}}$$

where β is the derived ratio of Fresnel reflection coefficients for surface scattering only, θ_i is the incidence angle, and ϵ_r is the dielectric constant. This equation can then be numerically solved to find the real part of the dielectric constant on a pixel-per-pixel basis.

Results and Discussion: This process was used to numerically solve for the dielectric constant with Mini-RF monostatic X-band baseline collects taken in the regions mentioned previously.. The number of baseline collects across each region were: Faustini (10), Shoemaker (16), Haworth (14), Sverdrup (14). These collects were then transformed from a line/sample to latitude/longitude coordinate system, and we superimposed bounds from [3] for each respective region. This gave us the ability to look at basic statistics for regions within the bounds compared to the image average (referred to as "full"). Figure 1a shows an example collect of the S1 stokes parameter with the bounds for Shoemaker crater. A subset of the collect is shown in Figure 1b along with the dielectric constant inversion in Figure 1c. Note that our numerical solver could not converge on every pixel, and we assigned *NaN* values wherever this occurred (these pixels show up as fully black on the inversion images). This is an ongoing

issue which we are trying to address by using other numerical solvers. The results for all inversions across the four regions are summarized in Table 1, where averages and standard deviations of every collect for a given region are listed.

Region	ϵ_r (Avg.)	ϵ_r (Std. Dev.)
Faustini (full)	2.952	0.0542
Faustini (bounds)	2.798	0.1009
Shoemaker (full)	2.943	0.0580
Shoemaker (bounds)	2.658	0.1180
Haworth (full)	2.976	0.0460
Haworth (bounds)	2.820	0.1440
Sverdrup (full)	2.997	0.1107
Sverdrup (bounds)	2.943	0.2289

Table 1: Average and standard deviation values of inverted dielectric constant from all Mini-RF X-band baseline collects going over each respective region.

Faustini, Shoemaker, and Haworth show a significant average decrease in ϵ_r of 0.154, 0.285, and 0.156 respectively, when comparing the specified crater bounds to the entire region. Sverdrup shows almost no difference comparatively. To interpret these results, we turn to modeled mixtures of water-ice and lunar/planetary regolith. In general, dielectric constant is expected to decrease for regions with porous water-ice because porous water-ice has $\epsilon_r \approx 2.0$ [10] which is lower than that of laboratory measurements of pure lunar regolith analog material $\epsilon_r \approx 5$ [11]. Furthermore, the Lyman Alpha Mapping Project (LAMP) on LRO has also consistently measured a higher porosity for PSR regions compared to non-PSR regions [12]. Thus, to first order, our results are consistent with the premise that surficial water-ice exists in Faustini, Shoemaker, and Haworth. However, the results are not consistent for Sverdrup. Note that all four of these craters are comprised of the same type of geologic unit [13].

Acknowledgments: The authors would like to thank Scott Turner for helping with coordinate frame transformations. Data used were acquired from the Planetary Data System (PDS) Geosciences node.

References: [1] Nozette, S., et al. (2010) *Space Science Reviews 150(1)*, 285-302. [2] Li, S., et al. (2018) *Proceedings of the National Academy of Sciences, 115(36)*, 8907-8912. [3] Lemelin, M., et al. (2021) *The Planetary Science Journal, 2(3)*, 103. [4] Heggy, E., et al. (2020) *Earth and Planetary Science Letters, 541*, 116274. [5] Campbell, B. A. (2002) *Radar remote sensing of planetary surfaces*. [6] Olhoeft, G. R., et al. (1973) *Lunar and Planetary Science Conference Proceedings* (Vol. 4, p. 3133) [7] Fa, W., et al. (2011) *Journal of Geophysical Research: Planets*, *116*(E3). [8] Elachi, C., Van Zyl, J. J. (2006) *Introduction to the physics and techniques of remote sensing*. [9] Kumar, A., et a. (2021) *IEEE Transactions on Geoscience and Remote Sensing*. [10] Heggy, E., et al. (2019) *Monthly Notices of the Royal Astronomical Society, 489(2)*, 1667-1683. [11] Heggy, E., et al. (2007) *Lunar and Planetary Science Conference* (No. 1338, p. 1756). [12] Gladstone, G. R., et al. (2012) *Journal of Geophysical Research: Planets, 117*(E12). [13] Fortezzo, C. M., et al. (2020) *Unified Geologic Map of the Moon*.

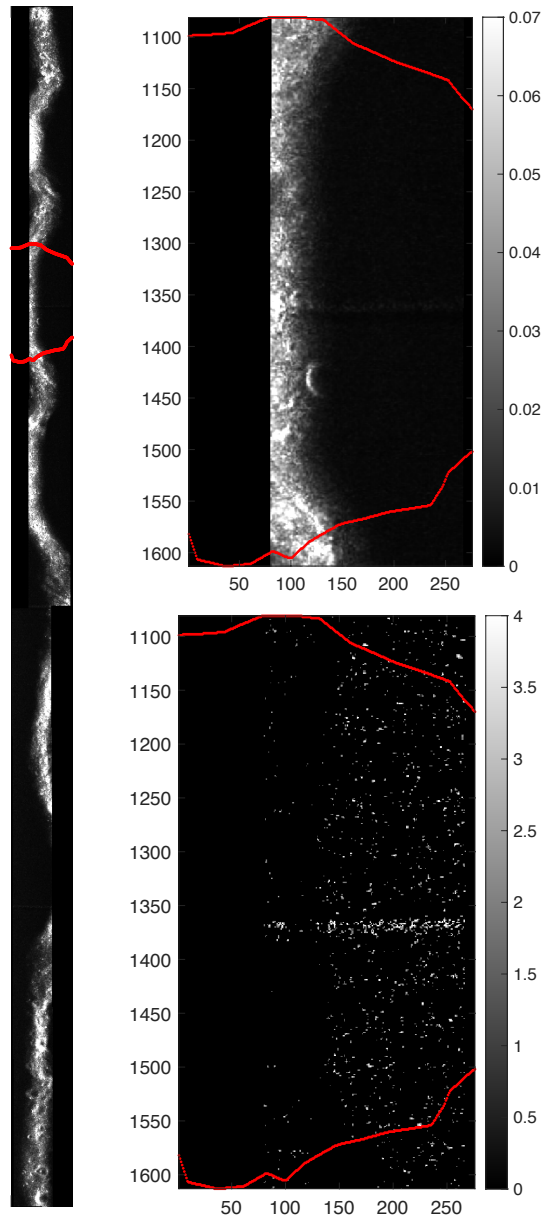

Figure 1: **(a)** Left: S1 Stokes parameter product of *lxb_00771_2cd_oiu_86s341_v1* showing Shoemaker bounds from [3]. **(b)** Top Right: A zoomed-in version of 1a. **(c)** Bottom Right: A zoomed-in version of 1a showing dielectric constant inversion using the method outlined in [9].